Low consumption Fenton-like water purification through pollutants as electron donors substituting H_2O_2 consumption via twofold cation-π over MoS_2 cross-linking g-C_3N_4 hybrid

Lai Lyu [a,b], Chao Lu [a], Yingtao Sun [a], Wenrui Cao [a], Tingting Gao [a], Chun Hu [a,*]

[a] Key Laboratory for Water Quality and Conservation of the Pearl River Delta, Ministry of Education, Institute of Environmental Research at Greater Bay, Guangzhou University, Guangzhou 510006, China
[b] Institute of Rural Revitalization (Guangdong Province), Guangzhou University, Guangzhou 510006, China

ABSTRACT

A twofold cation-π-assembled catalyst consisting of honeycomb microsphere-like MoS_2 cross-linking g-C_3N_4 hybrid (HM-MS/CN) is first developed to address the bottleneck of excessive resource and energy consumption in Fenton chemistry. A series of modern characterization techniques combined with theoretical calculation are used to reveal and verify the twofold cation-π interaction (Mo-O-C and Mo-S-C bonding bridges). It is found that the electrons of pollutants can be captured by H_2O_2 and O_2 through the twofold cation-π interaction during Fenton-like reaction, which inhibits the oxidative decomposition of H_2O_2 and promotes its hydroxylation. As a result, HM-MS/CN shows excellent performance for water purification by initiating pollutants as electron donors substituting H_2O_2 consumption under mild natural conditions, and the actual consumption of H_2O_2 in this system is only 6–8% of that in the common Fenton systems. This discovery is of great significance for the development of novel water purification technology with high efficiency and low consumption.

1. Introduction

Hydrogen peroxide (H_2O_2) is a nexus chemical that has been commonly used for chemical synthesis, pulp bleaching industry, and wastewater treatment [1–5]. As an important chemical resource, its annual production has exceeded 3 million tons [3]. The current H_2O_2 production process is an indirect, energy-demanding, and waste-intensive anthraquinone route [1], which leads to a large amount of resources and energy consumption [3,6]. For the application industry of H_2O_2 involved in hydroxylation process, the excessive consumption is still everywhere due to nonselective oxidation and reduction of H_2O_2 by the surface metal sites on the catalyst, which leads to the cleavage of O-O and O-H bonds of H_2O_2 after obtaining/losing electrons or energy [7]. In particular, the invalid decomposition of H_2O_2 is widely present in Fenton/Fenton-like reaction for wastewater treatment [8,9], in which H_2O_2 acts as electron acceptors being reduced to hydroxyl radicals (•OH) through cleaving O-O bonds and also acts as electron donors being oxidized to superoxide radicals ($HO_2^•/O_2^{•-}$) or even O_2 via breaking apart O-H bonds [10–19]. The whole redox process consumes a large excess of H_2O_2 (above the stoichiometric amount by 100-fold) [20]. Therefore,

reforming the technological process of H_2O_2 application to reduce its consumption and enhance the catalytic performance is of great significance for the whole H_2O_2 industry.

Ma et al. used a cocatalyst of FeP and trace Fe^{2+} to speed up the electron cycle in Fenton reaction, which enhanced the decomposition efficiency of H_2O_2 and accelerated the degradation of methylene blue [21]. Zheng et al. reported that MoS_2 co-catalyst was introduced into the multifunctional catalytic membrane [22]. The proposed synergistic effect led to the efficient activation of H_2O_2 and the production of more •OH. Bai et al. prepared $Mo_{1-x}S_{2-y}$ photocatalysts with S-vacancies to achieve high innergenerate-H_2O_2 and degradation efficiency [23]. Sun et al. prepared the hetero-phase junction 1 T/2 H-MoS_2 @FeOOH with Fe^{2+}/Fe^{3+} and Mo^{4+}/Mo^{6+} reaction sites, which were beneficial for the efficient activation of H_2O_2 to $HO_2^•/O_2^{•-}$ in a photo-Fenton process [24]. These studies have taken into account the effective utilization of H_2O_2 and provided strategies for enhancing the production of free radicals.

Our previous studies have shown that the intermediate organic radicals and peroxide radicals produced by the chain reaction between organic compounds and •OH can be used as substitutable electron donors to hinder the semi-reaction of H_2O_2 oxidation, which greatly

---

* Corresponding author.
E-mail address: huchun@gzhu.edu.cn (C. Hu).

depends on the construction of the dual-reaction-centers (DRCs) with electron distribution-polarized micro-areas on the catalyst surface [11, 14,25–30]. It was found that H_2O_2 was mainly reduced to $^\bullet OH$ in the electron-rich centers without exchanging electrons with electron-deficient sites. On the contrary, the electrons of the activated intermediate organics were captured by the electron-deficient centers and transferred to electron-rich centers through the formed cation– π bridges, which greatly increased the activity of Fenton-like reaction and decreased the consumption of H_2O_2 [27]. This process even induces an oxygen activation process that produces $HO_2^\bullet/O_2^{\bullet-}$, H_2O_2 and $^\bullet OH$ in situ [31,32], similar to the oxygen reduction process [33], but without the introduction of external energy, significantly reducing resource and energy consumption in wastewater treatment. Obviously, the key to the success of this process lies in the rational construction of the cation– π bridges for oriented electron transfers [34].

Cation– π interaction is an important noncovalent force caused by the electrostatic attraction between a metal cation and a π electron system that influences the structures and functions of a variety of molecules and materials [35–37]. It has been found that coordination of negatively charged ligands to the M^+ could affect the activity to be suitable for the cation– π interaction [36]. This is mainly due to the orbital interactions involving electron transfer of $\pi \rightarrow M^+$ (σ donation) or $M^+ \rightarrow \pi^*$ (π back-donation) [38]. Therefore, to realize the direct utilization of the alternative inert electron donors (e.g. refractory organic pollutants) and decrease the consumption of H_2O_2 during the DRCs process, the key is to enhance the cation– π interaction for electron transfer through constructing delocalized bonding bridge on the catalyst surface.

Herein, a novel DRCs-catalyst consisting of honeycomb microsphere-like MoS_2 cross-linking g-C_3N_4 hybrid (HM-MS/CN) with the special cation-π structures enhanced by twofold electron transfer bonding bridge (Mo-O-C and Mo-S-C) is successfully fabricated. It is found that this surface structure can directly capture the electrons from the stable organic compounds and transfer these electrons to dissolved oxygen (DO) under natural air conditions. In the presence of H_2O_2, the activated electrons are quickly captured by H_2O_2, which controls the disproportionation reaction and makes the hydroxylation of H_2O_2 become the dominant reaction. Based on this principle, in the field of water treatment, different refractory organic pollutants, such as synthetic dyes rhodamine B (RhB) [39], pesticide precursor 2-chlorophenol (2-CP), plasticizer and endocrine disruptor bisphenol A (BPA) [40,41], fluoroquinolone antibiotics ciprofloxacin (CIP) [42] and alkaline biological azo dye methylene blue (MB) [43] (see Fig. S1 in the Supporting Information), can be rapidly degraded in the HM-MS/CN/H_2O_2 system. The reaction rate is ~39 times higher than that of the conventional system. Refractory pollutants as spontaneous electron donors substituting H_2O_2 consumption via the twofold cation-π is successfully realized, which is equivalent to achieving twice hydroxylation role for every one H_2O_2 molecule consumption. The actual consumption of H_2O_2 in this system is only 6–8% of that in the conventional technologies. A novel interfacial mechanism of the reaction system has also been proposed and demonstrated in this work.

2. Experimental section

The chemicals and reagents, synthesis details, characterization and analysis methods, and calculation methods are described in Supporting Information.

As a typical experiment process, 0.06 g catalyst powder was added in 100 mL pollutant solution and magnetically stirred for 20 min to establish the adsorption-desorption equilibrium under natural conditions. Then the Fenton-like reaction was initiated by adding H_2O_2 solution (10 mM). At given time intervals, 2 mL aliquots were collected and filtered using a Millipore filter (pore size 0.45 μm) for analysis. The concentrations of RhB and MB were measured by the Hitachi Model UH4150 Spectrophotometer. The concentrations of 2-CP, BPA and CIP

were measured by a high performance liquid chromatography (HPLC, 1260 Infinity II; Agilent) with an auto-sampler, a Poroshell 120 EC-C18 column (4.6 ×100 mm, 2.7 μm) and an UV detector. The mobile phase was a mixture of methanol/water and was operated at a flow-rate of 1.0 mL min^{-1}. The H_2O_2 concentration was determined using the reported *N, N*-diethyl-*p*-phenylenediamine sulfate (DPD) methods [44]. The total organic carbon (TOC) was determined by a TOC-L CPH CN200 analyzer (Shimadzu) using high-temperature combustion. The amount of metallic ions in the solutions were measured using the inductively coupled plasma mass spectrometry (ICP-MS) on a NexION 300 (PerkinElmer, U. S.A.). To test the recyclability of HM-MS/CN, the used samples were filtered, washed and dried at 70 °C, and were reused in following cycle. The EPR spectra were recorded on a Bruker A300–10/12 EPR spectrometer under natural conditions. 5-Tert-butoxycarbonyl-5-methyl-1-- pyrroline-N-oxide (BMPO)-trapped EPR signals were detected in different air-saturated methanol/aqueous dispersions of the corresponding samples: 0.01 g of the prepared powder sample was added to 1 mL methanol (for detecting $O_2^{\bullet-}$) or water (for detecting $^\bullet OH$); 100 μL of the above suspension, 10 μL of BMPO (250 mM) and 10 μL of H_2O_2 (30%, w/w, if needed) were mixed and held for 5 min. The solution was sucked into the capillary to carry out the detection.

3. Results and discussion

3.1. Synthesis and characterization of HM-MS/CN

The typical synthesis route of HM-MS/CN involves the following steps as schematically illustrated in Fig. 1. In the first step, g-C_3N_4 was prepared by the thermal polymerization of the urea precursor. Then, the obtained g-C_3N_4 were homogenously dispersed into sodium molybdate dihydrate ($Na_2MoO_4 \bullet 2 H_2O$) and thiourea (CH_4N_2S) aqueous solution. The mixture was alternately stirred and sonicated, followed by the hydrothermal self-assembly process in the Teflon-lined autoclaves. MoS_2 gradually grows to form crystals on the g-C_3N_4 substrates and finally embedded in each other to form the honeycomb microsphere-like cross-linking HM-MS/CN hybrid in the hydrothermal environment. As a reference, the pure MoS_2 was also synthesized as described above without the addition of g-C_3N_4.

Scanning electron microscopy (SEM) images (Fig. 2a-c) show that HM-MS/CN possesses an aesthetical 3D honeycomb microsphere-like structure. The diameter of the HM-MS/CN microsphere is 1–2 μm, which are composed of the well-dispersed nanosheets with a plentiful number of cracks and gaps. Transmission electron microscopy (TEM) images (Fig. 2d,e) show that the crumpled nanosheets of the HM-MS/CN microsphere with plenty of folded edges are semitransparent under the electron bundle. The high resolution transmission electron microscopy (HRTEM) image (Fig. 2f) shows that the black lines are parallel layers of MoS_2 nanosheets perpendicular to the (002) direction with the interlayer distance of 0.625 nm [45], which is the principal crystalline phase characteristic of HM-MS/CN from the images. In addition, some narrower shallow lattice stripes with the lattice spacing of 0.27 nm also can be observed, which correspond to the (100) crystal facets of MoS_2. g-C_3N_4 with distinct shades and without obvious exposure of crystal facets attaches tightly to the MoS_2 lamellar structure, indicating that MoS_2 has constructed complex heterojunctions with g-C_3N_4 in HM-MS/CN [46]. The element mappings of HM-MS/CN (Fig. 2g) confirm the presence of the Mo, S, C, N and O elements and the well dispersions of the five elements in the sample, indicating that the combination of g-C_3N_4 and MoS_2 is very uniform and pyknomorphic and the O species are very closely involved in their integration during the fabrication process of HM-MS/CN.

The powder X-ray diffraction (XRD) profiles for g-C_3N_4, MoS_2 and HM-MS/CN are shown in Fig. 2h. For g-C_3N_4, two peaks at 13.1 and 27.3 degree are assigned to the characteristic (100) and (002) planes, respectively [22,47]. For the pure MoS_2, the diffraction peaks at 16.8, 32.6 and 57.1 degree are attributed to the (002), (100) and (110) crystal
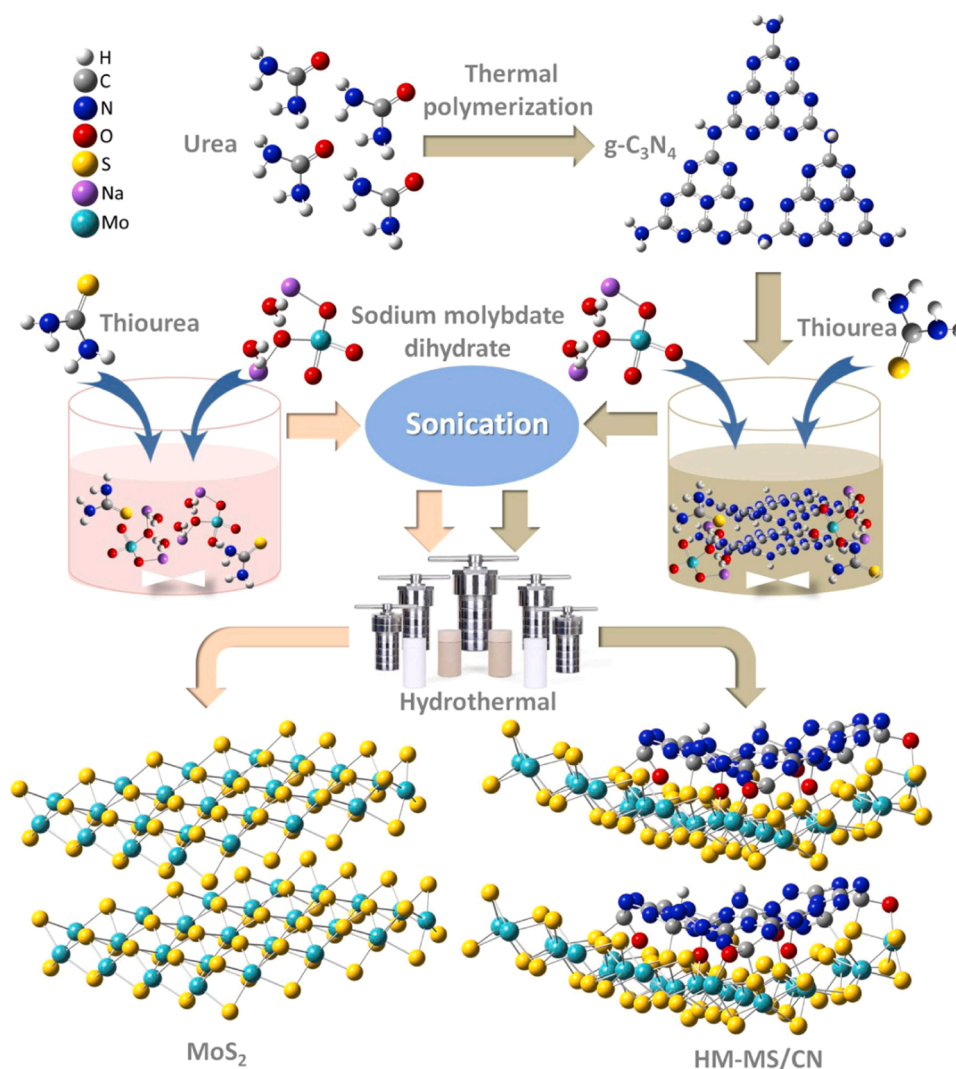
Fig. 1. Schematic illustration for the synthesis routes of the pure MoS_2 and HM-MS/CN.

planes [48], respectively. Very differently, after integration of the two species, the characteristics of the crystalline phase changed obviously. For HM-MS/CN, although the main structure features of g-C_3N_4 was retained, the (002) plane belonging to g-C_3N_4 disappeared, indicating the strong hybridization of MoS_2 on the (002) plane of g-C_3N_4, which also affected the crystalline of MoS_2 that the (100) and (110) peaks shifted to higher 2θ angles. Combined with the HRTEM image above, the diffraction peak at 13.9 degree on HM-MS/CN XRD pattern is attributed to the dominant (002) crystal planes, which obviously shifted to a much lower 2θ angle by 2.9 degree compared with that of the pure MoS_2, implying a change in interlayer spacing due to the chelation and hybridization of the carbon and nitrogen species. Fig. 2i shows the Raman spectra of MoS_2 and HM-MS/CN. The two dominant peaks of the pure MoS_2 at 375 and 403 cm^{-1} are associated with the in-plane E_{2g}^1 and out-of-plane A_g^1 modes of MoS_2, respectively. It has been reported that the peak frequency difference (Δ) between A_g^1 and E_{2g}^1 modes can be used to identify the layer number of MoS_2 [48]. The value of Δ reduces to 26 cm^{-1} from 28 cm^{-1} after chelating with g-C_3N_4, confirming that the MoS_2 nanosheets in the HM-MS/CN hybrid are more delaminated with mainly few layers. Another very critical information is that the A_g^1 vibration mode is obviously enhanced for HM-MS/CN compared with that of the pure MoS_2, which indicates that the chelated g-C_3N_4 strongly pulls the S atoms on the surface of MoS_2, resulting in the violent vibration of the out-of-plane A_g^1 modes in the hybrid, implying the bonding of S and

g-C_3N_4. For the high resolution X-ray photoelectron spectroscopy (XPS) spectra of HM-MS/CN, the position and shape of the Mo 3d doublets confirm that the MoS_2 species in HM-MS/CN have two polymorphs (2 H and 1 T) and are present predominantly as the semiconducting 2 H phase with trigonal prismatic coordination (Fig. S2) [49,50]. However, the pure MoS_2 are present mainly as the metallic 1 T phase (Fig. S3), which suggests the prominent phase transition of the formed MoS_2 under the interference and hybridization of g-C_3N_4 during the fabrication process of HM-MS/CN. The Mo 3d XPS spectrum of HM-MS/CN (Fig. S2) can be deconvoluted into six peaks, and one of those at 225.4 eV actually corresponds to S 2 s. The main intense Mo $3d_{5/2}$ (227.9 and 228.6 eV) and Mo $3d_{3/2}$ (231.1 and 231.7 eV) components are Mo(IV) characteristic of MoS_2. The high binding energy peak of Mo 3d (235.0 eV) corresponds to Mo(VI), owing to the existence of trace of surface oxide species [51]. The S 2p XPS spectrum of HM-MS/CN (Fig. 2j) at 161.2 and 162.4 eV correspond to the saturated basal-plane S atoms (S $2p_{3/2}$) and the unsaturated terminal S atoms (S $2p_{1/2}$) [52], respectively. Compared with the pure MoS_2 (Fig. S4), the binding energy peak of the unsaturated terminal S atoms is weakened obviously for HM-MS/CN, further confirming the bonding of the unsaturated terminal S atoms with the introduced g-C_3N_4. It is worth noticing that another new peak at 163.2 eV appears in the S 2p XPS spectrum of HM-MS/CN, which correspond to the S-C bonds resulting by the lattice S in the host g-C_3N_4 [53]. This result is further confirmed by
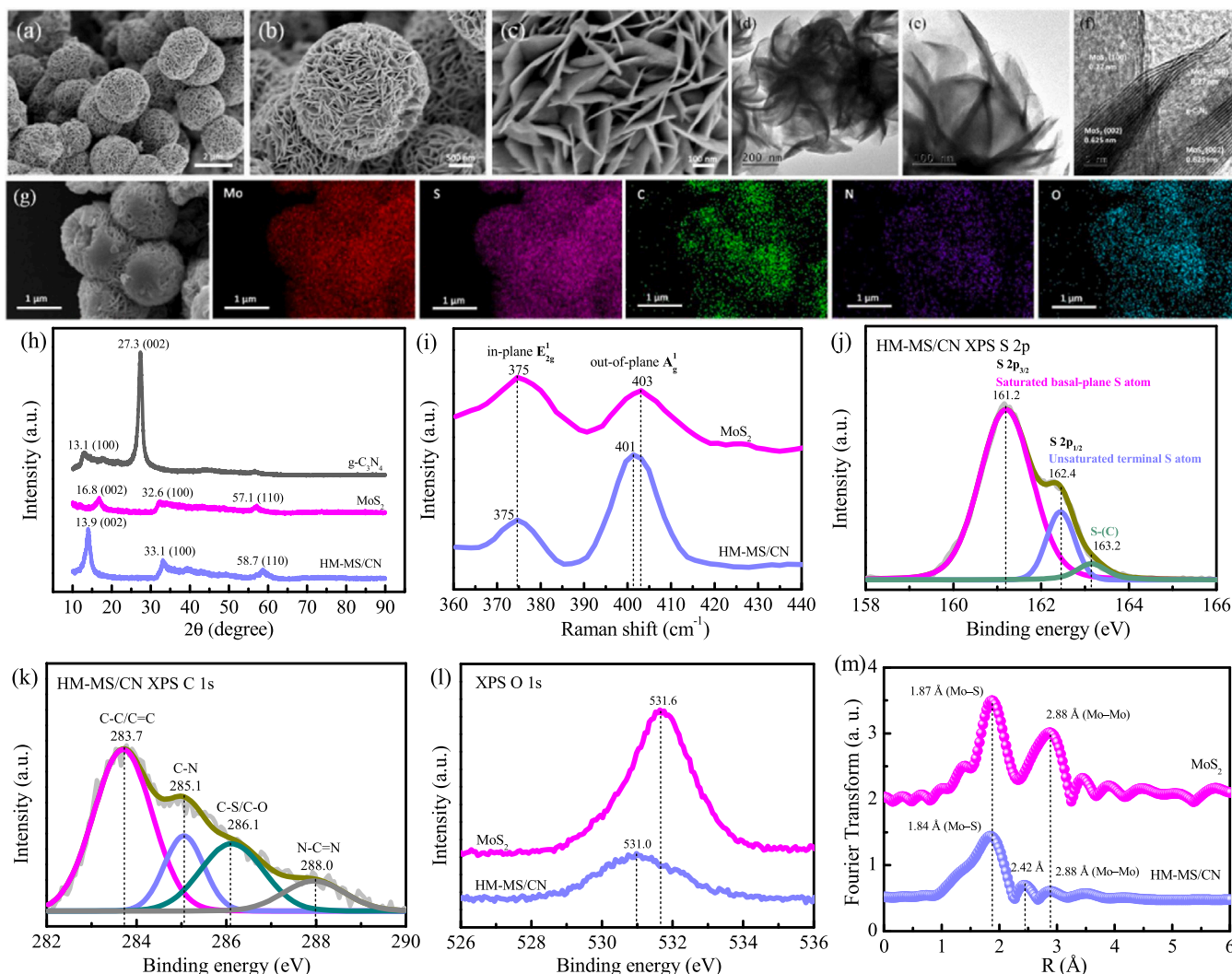
Fig. 2. (a), (b) and (c) SEM images of HM-MS/CN. (d) and (e) TEM images of HM-MS/CN. (f) HRTEM images of HM-MS/CN. (g) SEM elemental mapping analysis (Mo, S, C, N and O) of HM-MS/CN. (h) XRD patterns of g-C$_3$N$_4$, MoS$_2$ and HM-MS/CN. (i) Raman spectra of MoS$_2$ and HM-MS/CN. High-resolution XPS spectra in the (j) S 2p core levels of HM-MS/CN, (k) C 1 s core levels of HM-MS/CN and (l) O 1 s core levels of MoS$_2$ and HM-MS/CN. (m) Fourier transforms of k^3-weighted EXAFS oscillations obtained at the Mo K-edge of MoS$_2$ and HM-MS/CN.

the C 1 s XPS spectrum of HM-MS/CN (Fig. 2k). In addition to the characteristic peaks of C-C/C═C (283.7 eV), C-N (285.1 eV) and N-C≡N (288.0 eV) from g-C$_3$N$_4$, an obvious peak at 286.1 eV is also observed, which is attributed to the formed C-S and C-O bonds during the hybridization of g-C$_3$N$_4$ and MoS$_2$ [53]. Fig. 2l shows the O 1 s XPS spectra of MoS$_2$ and HM-MS/CN. The O 1 s peak of the pure MoS$_2$ locates at 531.6 eV, which may be originated from the surface oxygen (above 531.0 eV), including the surface hydroxyl and other chemisorbed oxygen species on the catalyst surface [29], because the pure MoS$_2$ itself does not exist lattice oxygen species. It is interesting that the O 1 s peak shifts to a much smaller binding energy (531.0 eV) corresponding to the lattice O species [54] for HM-MS/CN and the peak intensity is greatly weakened, which indicates that the surface O species on MoS$_2$ are substituted by g-C$_3$N$_4$ and form lattice oxygen (Mo-O-C) between MoS$_2$ and g-C$_3$N$_4$ in HM-MS/CN.

Fig. 2m shows the magnitude of the Fourier-transformed extended X-ray absorption fine structure (EXAFS) signals at the Mo K-edge of MoS$_2$ and HM-MS/CN. The EXAFS spectrum of HM-MS/CN shows the peaks at R′ = 1.84 and 2.88 Å (R′ being the apparent distance without phase correction and R being the actual distance obtained from curve fittings), corresponding to Mo−S and Mo−Mo interactions [55], respectively. The reduction of 3 Å of the Mo−S shell, the evident weakening of the

Mo−Mo interaction peak and the appearance of the new peaks (such as at 2.42 Å) for HM-MS/CN compared with that for the pure MoS$_2$ indicate the existence of other cation shells on HM-MS/CN, which obviously affect the local coordination environment of Mo. To reveal the fine coordination environment and obtain the precise structure parameters, we performed the advanced fittings for the EXAFS signals. As shown in Fig. S5, the fitting curves on [χ(R)] and Re[χ(R)] coincide with the corresponding experimental signals of HM-MS/CN in the key shell range of 0.5–3.5 Å and the R-factor is less than 0.02, which confirms the high credibility of the fitting results. The final fitting parameters are listed in Table 1. For the pure MoS$_2$, the first shell (Mo−S) from the Mo-S bonds with a bond distance (R) of 2.41 Å and a coordination number (CN) of 6.2 and the second shell (Mo−Mo) from the Mo-S-Mo bonds with R = 3.17 Å and CN = 6.0 are observed. For the first coordination shells of HM-MS/CN, the CN of Mo−S shell decreases to 3.6 and a new Mo−O shell with R = 1.64 Å and CN = 0.6 emerges, suggesting that oxygen atoms are introduced into the structure of HM-MS/CN to form Mo-O bands during the hybridization process and change the first shells through influencing the coordination of Mo to S. For the second coordination shells of HM-MS/CN, the R of Mo−Mo shell reduce to 3.08 Å and the CN significantly decreases to 0.6, which is due to that the intromittent g-C$_3$N$_4$ nanosheets and O atoms greatly hindered the

Table 1
Structural parameters obtained from Mo K-edge EXAFS fittings for MoS_2 and HM-MS/CN.

Sample	Shell	R (Å)[a]	CN[b]	σ^2 (Å^2)[c]	ΔE_0 (eV)[d]	R_f[e]
MoS_2	Mo−S	2.41	6.2	0.0019	-2.1	0.0061
	Mo−Mo	3.17	6.0	0.0019	-2.1	0.0061
HM-MS/CN	Mo−O	1.64	0.6	0.0083	-2.5	0.0194
	Mo−S	2.41	3.6	0.0083	-2.5	0.0194
	Mo−Mo	3.08	0.6	0.0083	-2.5	0.0194
	Mo−C	3.17	0.8	0.0083	-2.5	0.0194

[a] Bond distance
[b] Coordination number.
[c] Debye-Waller factor.
[d] Inner potential correction.
[e] Residual factor.

formation of Mo-S-Mo bonds, resulting in the Mo−Mo coordination layer being affected and weakened. One of the most important information is that the Mo−C shell (belonging to the second shells) from Mo-O-C bonds with R = 3.17 Å and CN = 0.8 is formed in the structure of HM-MS/CN. However, the coordination number of Mo to C (0.8) is larger than that of Mo to O (0.6), indicating that the observed Mo−C shell is not only the contribution of M-O-C, but also the contribution of Mo-S-C. These results demonstrate the formation of Mo-S, Mo-S-Mo, Mo-O, Mo-O-C and Mo-S-C bonds in HM-MS/CN and reveal the

cross-linking structure between MoS_2 and g-C_3N_4 in HM-MS/CN. The formation of the multiple cross-linking bond bridges can greatly accelerate the transfer of electrons through cation-π interactions over HM-MS/CN.

3.2. Surface electron distribution through DFT calculation

The optimized geometry structures and the corresponding two-dimensional valence-electron density color-filled maps of the HM-MS/CN models by DFT calculations are shown in Fig. 3. The geometry optimizations and property calculations were performed by using Gaussian 03 package. The dangling bonds were terminated with H atoms to obtain a neutral cluster. From the view of the Mo-O-C plane fragment (Fig. 3a), we can see that the structure of MoS_2 substrate has been deformed to some extent due to the influence of the formed Mo-O-C and C-S bonds, which is consistent with the above characterization results. In the corresponding two-dimensional valence-electron density color-filled map (Fig. 3b), the largest electron distribution area appears around the Mo atom (Mo1, Mulliken charge 1.27) on Mo-O-C bond, and its maximum valence-electron density (relative value) is as high as 1.0 e/Å^3, which is obviously higher than that (~0.8 e/Å^3) of the normal Mo atom (Mo2, Mulliken charge 1.06) without connecting g-C_3N_4. This result indicates that the surface complexation of g-C_3N_4 on MoS_2 activates the π electrons, which are transfer to the periphery of Mo due to π→Mo (σ
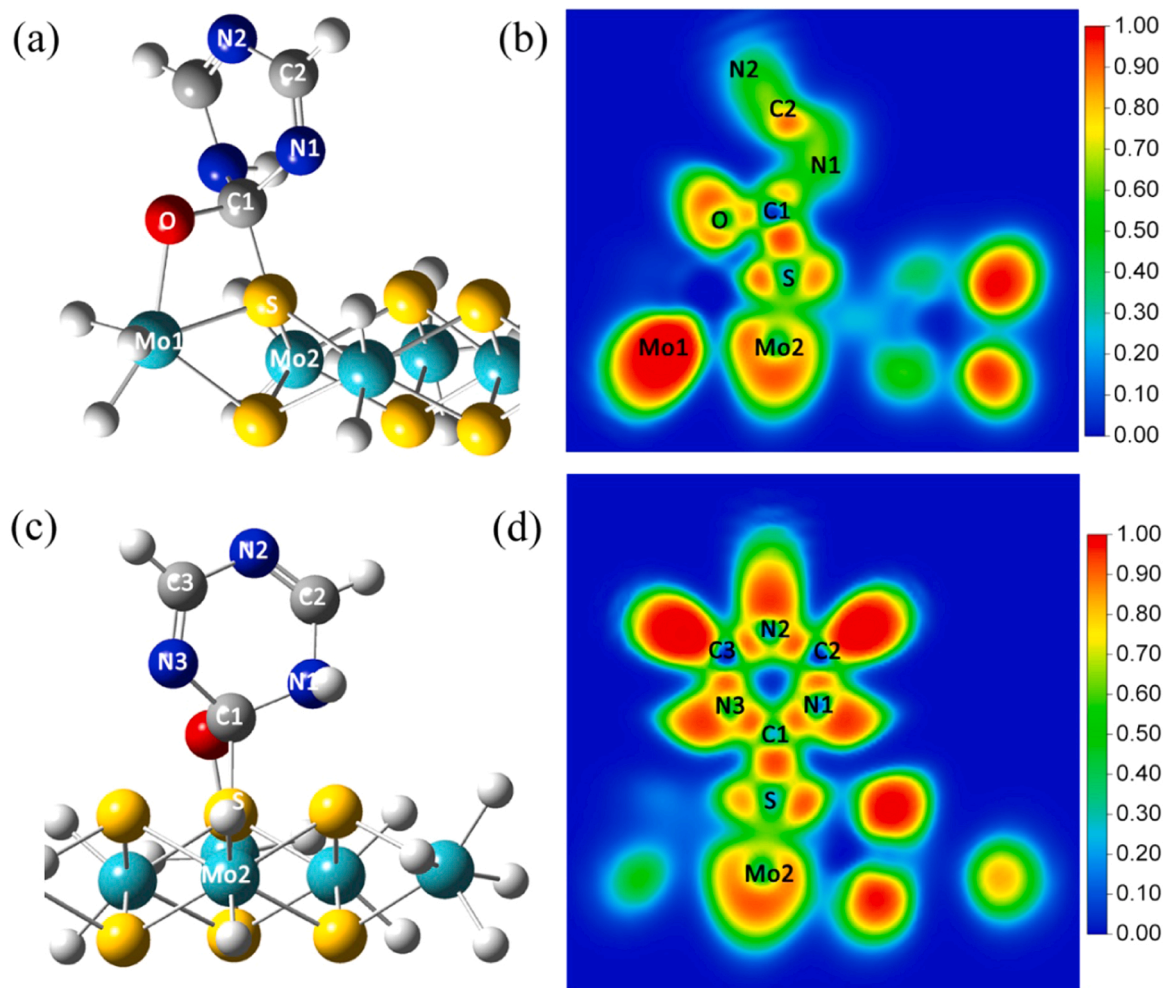

Fig. 3. (a) The optimized structure of HM-MS/CN in Mo-O-C plane fragment with (b) the corresponding two-dimensional valence-electron density color-filled map in Mo-O-C plane fragment, and (c) the optimized structure of HM-MS/CN in g-C_3N_4 plane fragment with (d) the corresponding two-dimensional valence-electron density color-filled map in g-C_3N_4 plane fragment of HM-MS/CN by DFT calculations. Cyan, yellow, red, gray, blue and white circles denote Mo, S, O, C, N and H atoms, respectively. The valence-electron density is given in e/Å^3.

donation) through the two bonding bridges (C-O-Mo and C-S-Mo), resulting in the formation of electron-rich Mo centers in HM-MS/CN. Fig. 3c,d show the optimized structure and the corresponding valence-electron density distribution of HM-MS/CN in the g-C$_3$N$_4$ plane fragment. Obviously, the C atom (C1) on the C-O-Mo and C-S cross-linking bridges shows the narrowest electron distribution area and a lower valence-electron density compared with that of the N atoms (N1, N2 and N3) and the other C atoms (C2 and C3) without connecting Mo and S on the hexatomic ring, indicating that the electron-deficient sites is also formed around the C1 atom due to the π→Mo interactions on HM-MS/CN. These results demonstrate the formation of surface DRCs on HM-MS/CN through construction of cation-π structures enhanced by the twofold electron transfer bonding bridges involving in Mo-O-C and Mo-S-C.

3.3. Excellent performance for pollutant degradation

Pesticides, pharmaceuticals, endocrine disrupting chemicals and dyes, which are highly toxic and stable organic compounds, are selected to evaluate the performance of the prepared catalysts with H$_2$O$_2$ at natural pH without any extra energy input. For the degradation of the carcinogenic dyestuff rhodamine B (RhB), the tested samples exhibit very different activity. As shown in Fig. 4a, only 27.3% of RhB is removed within 30 min over the conventional Fe$_3$O$_4$ Fenton-like process. Obviously, the activity of Fe$_3$O$_4$ is seriously inhibited under neutral conditions. RhB removal is 10.1% and 74.2% in the solitary g-C$_3$N$_4$ and the pure MoS$_2$ suspensions, respectively, under the same conditions. Astonishingly, in the HM-MS/CN suspension, RhB removal reaches 98.6% within only 10 min and the pollutant can be completely degraded at 15 min, which is ~39, 102 and 9 times higher than that in the suspensions of Fe$_3$O$_4$, g-C$_3$N$_4$ and MoS$_2$, respectively (Fig. 4a insert). The TOC removal rate could reach ~64% in the HM-MS/CN suspension within 30 min, which was greatly higher than that in the suspensions of Fe$_3$O$_4$ suspension (TOC removal rate < 10%). For the degradation of other refractory pollutants, such as the pesticide 2-CP, endocrine disruptor BPA, pharmaceutical CIP and dyestuff MB, HM-MS/CN also exhibited excellent activity. As shown in Fig. 4b, all the refractory compounds were substantially degraded and the degradation rate could exceed 90% within 90 min. Especially for CIP and MB, the degradation rate could respectively reach 90.1% and 88.2% within only 30 min. Even though MB has the property of quenching free radicals, it is still rapidly degraded, suggesting a new degradation pathway due to the constructed twofold cation-π interaction.

After the reaction, the concentration of dissolved Mo in the HM-MS/CN suspension is only 0.025–0.065 mg L^{-1}. We use the filtrate (with the maximum Mo ions 0.065 mg L^{-1}) to decompose the pollutants and no significant degradation is observed (Fig. S6), suggesting that the observed pollutant removals in HM-MS/CN suspension is attributed to the heterogeneous catalytic reactions and the contribution of the released Mo species is negligible. The durability of HM-MS/CN was tested after recovering the solid catalyst through filtration, washing and drying (Fig. S7). There was no obvious deactivation of the catalyst compared with the first Fenton-like reaction. The removal rate of RhB can reach ~95% within 15 min even after 7 successive cycles of degradation testing. Hence, HM-MS/CN is an efficient catalyst with a good repeatability and stability. Fig. 4c shows the effect of the initial pH value on RhB degradation in the HM-MS/CN suspension. In a very wide pH range (3.1–9.3), the degradation rate varies little, which indicates that the activity of the HM-MS/CN/H$_2$O$_2$ system is not obviously influenced by the pH values, revealing the wide applicable range of pH for HM-MS/CN. The reactivity of the metal-containing catalyst often strongly depends on the solution pH due to the formation of the surface hydroxyl groups by the dissociative chemisorption of water molecules in aqueous solution [56], while HM-MS/CN avoid this effect due to the rapid transfer of electrons by the cation-π interactions through the formed twofold cross-linking bond bridges.

Fig. 4d shows the actual and stoichiometric consumption curves of H$_2$O$_2$ and the corresponding utilization efficiency of H$_2$O$_2$ (calculation method and process are shown in the Supporting Information) in the HM-MS/CN Fenton-like system. In the first 30 min, the actual consumption of H$_2$O$_2$ is very close to its stoichiometric consumption. The utilization efficiency of H$_2$O$_2$ is above 86% prior to the complete disappearance of RhB (before 15 min), which is due to the provision of electrons from pollutants, avoiding the oxidation of H$_2$O$_2$. This is equivalent to achieving more than twice hydroxylation role for every one H$_2$O$_2$ molecule consumption. After that, the utilization efficiency of H$_2$O$_2$ begins to slowly decline due to the complete degradation of the refractory pollutants (the electrons provided by the pollutants are reduced), reaching 68.7% at 60 min, which is still much higher than the value (~5%) of the conventional Fe$_3$O$_4$ Fenton system [57]. Since the pollutants directly replace H$_2$O$_2$ as electron donors via the twofold cation-π interaction throughout the process, the consumption of H$_2$O$_2$ in this system is only 6–8% of that in the conventional technologies.

Actual water from the Pearl River was also collected and used to evaluate the activity and efficiency of HM-MS/CN. As shown in Fig. 4e, very strong signals corresponding to natural organic matter (NOM) was detected in the actual Pearl River water by EEM fluorescence spectra technology, especially the peak at λEX/λEM = 250/400 nm corresponding to tyrosine, soluble microbial and by-product substances showed the strongest fluorescence signal. After reaction in the HM-MS/CN system with trace amount of H$_2$O$_2$ (1 mM), the signal was significantly reduced (Fig. 4f), suggesting that the actual natural Pearl River water sample was deeply purified by HM-MS/CN. HM-MS/CN is also used to purify the RhB-contaminated river water (Fig. 4g). Surprisingly, the refractory RhB can be prioritized for removal from the RhB-NOM-combined polluted water with trace amount of H$_2$O$_2$ (Fig. 4h), thus achieving a rapid reduction in the toxicity of the water, which proves that the catalyst is highly efficient for actual water purification with low energy consumption. This rapid purification and low consumption of H$_2$O$_2$ may be caused by the polar complexation of pollutants with NOM, which enhances the interfacial electron transfer between organic matter and catalyst.

3.4. Interfacial reaction mechanism involving catalyst/H$_2$O$_2$/pollutants

To investigate the interaction of stable organic compounds/H$_2$O$_2$ with the polarized adsorption sites on HM-MS/CN, DFT calculation methods are further utilized. As shown in Fig. 5, we performed the adsorption/reaction of the typical fragment of hydroxylated organic molecule (stable phenol model) on the HM-MS/CN surface at two different sites, including the electron-deficient C site (Site 1) and the electron-rich Mo site (Site 2). According to the DFT calculation, phenol can be adsorbed stably at Site 1, but its adsorption at Site 2 is unstable. Then, we performed the adsorption/reaction of H$_2$O$_2$ molecule at the two different sites. Conversely, H$_2$O$_2$ cannot be adsorbed stably at Site 1, but its adsorption at Site 2 is very stable. The DFT total energy E(total) and adsorption energy ΔE(ads) for organic compound fragment and H$_2$O$_2$ at the two sites are shown in the table of Fig. 5. Obviously, H$_2$O$_2$ possesses the most negative adsorption energy (−1.61 eV) in Site 2, indicating that the adsorption of H$_2$O$_2$ is most stable at this site, which demonstrates theoretically that H$_2$O$_2$ does tend to combine with the electron-rich Mo sites to undergo a reduction reaction. However, organic compound molecule possesses the most negative adsorption energy (−0.43 eV) in Site 1 and the most positive adsorption energy (0.43 eV) in Site 2, indicating that the adsorption of organic compound is most stable at the electron-deficient C site (Site 1) on the aromatic-like CN-ring of HM-MS/CN and organic compound hardly interact with Mo site. This result demonstrates theoretically that organic compounds tend to react with the electron-deficient C sites on the aromatic-like CN-ring and provide electrons for the electron-deficient centers though π-π interactions.

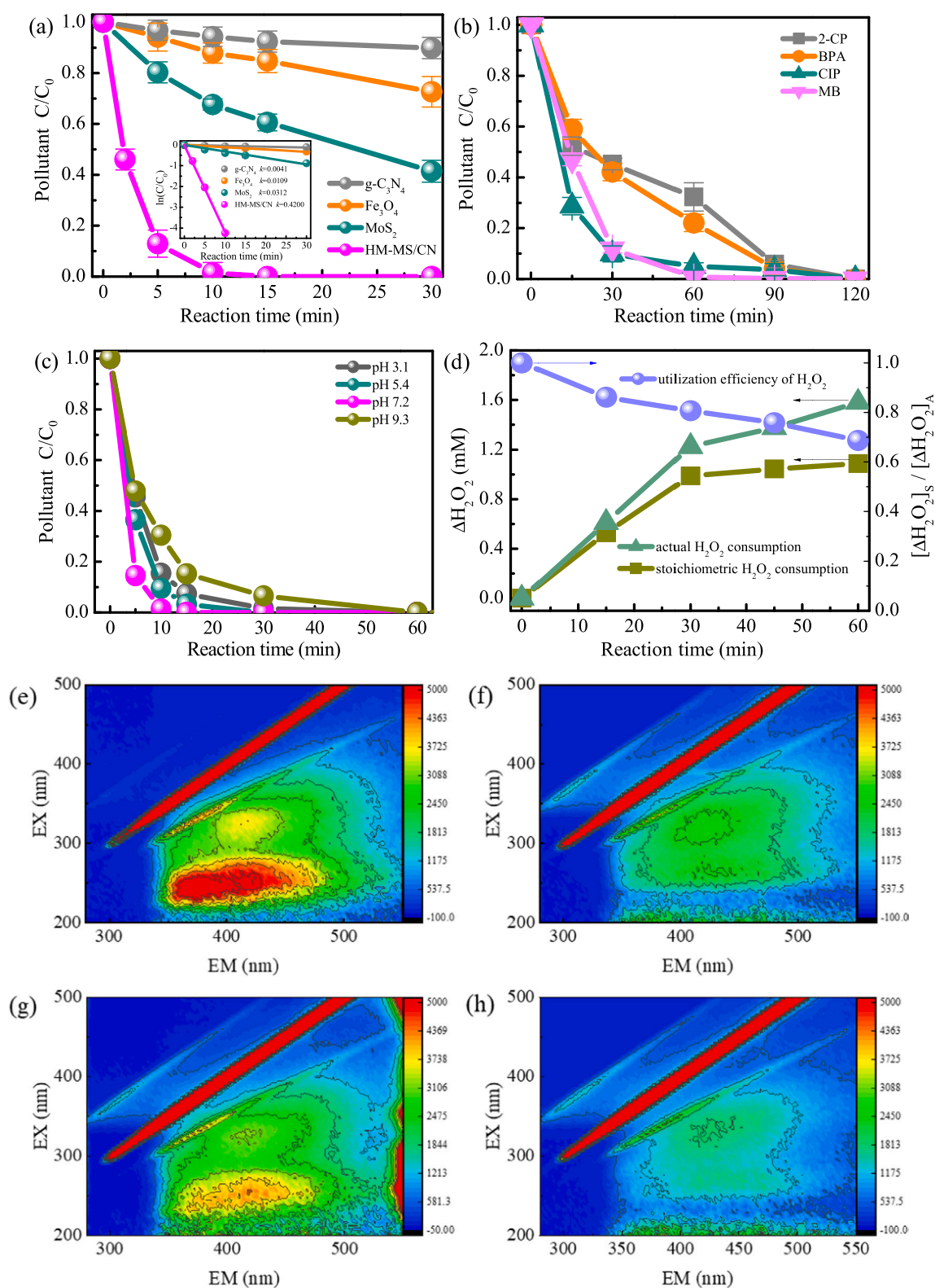The FTIR spectra of the pure MoS$_2$ sample, fresh HM-MS/CN and the

Fig. 4. (a) RhB degradation curves in various suspensions with H_2O_2. (Insert shows the corresponding kinetic curves). (b) Decomposition curves of other different refractory pollutants in the HM-MS/CN suspensions with H_2O_2. (c) Effect of initial pH values for RhB degradation in the HM-MS/CN suspension with H_2O_2. (d) Actual and stoichiometric H_2O_2 consumptions and the utilization efficiency of H_2O_2 during RhB degradation in the HM-MS/CN suspension. Reaction conditions: Natural initial pH (except c), initial [pollutant] = 10 mg L^{-1}, initial [H_2O_2] = 10 mM, [catalyst] = 0.2 g L^{-1} (for RhB degradation) or 0.6 g L^{-1} (for other pollutant degradation). EEM fluorescence spectra of the actual Pearl River water (e) before and (f) after purification by HM-MS/CN with H_2O_2. Reaction conditions: initial [H_2O_2] = 1 mM, [catalyst] = 0.3 g L^{-1}. EEM fluorescence spectra of the actual Pearl River water contaminated by RhB (g) before and (h) after purification by HM-MS/CN with H_2O_2. Reaction conditions: initial [RhB] = 5 mM, initial [H_2O_2] = 1 mM, [catalyst] = 0.3 g L^{-1}.

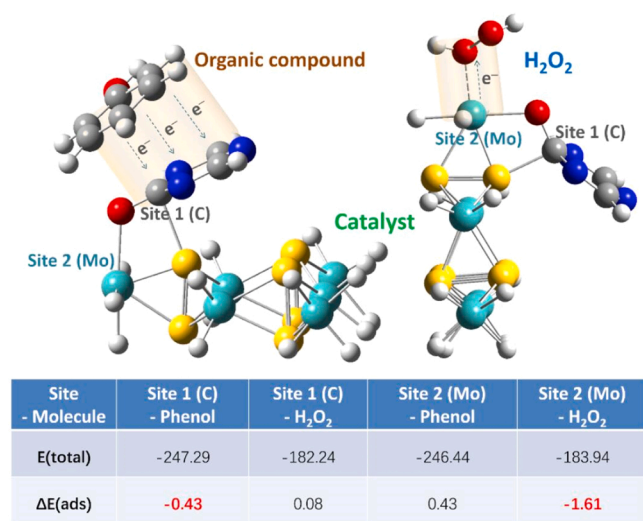| Site - Molecule	Site 1 (C) - Phenol	Site 1 (C) - H_2O_2	Site 2 (Mo) - Phenol	Site 2 (Mo) - H_2O_2
E(total)	-247.29	-182.24	-246.44	-183.94
ΔE(ads)	**-0.43**	0.08	0.43	**-1.61**

Fig. 5. Optimized adsorption/reaction model for organic compound (phenol fragment) and H_2O_2 on the surface of HM-MS/CN, as well as the DFT total energy E(total) and adsorption energy ΔE(ads) for pollutant and H_2O_2 molecules at different sites on the surface of HM-MS/CN by DFT calculations. Unit: eV. Calculation method: ΔE(ads)=E(total)-E(base)-E(mol). Cyan, yellow, red, gray, blue and white circles denote Mo, S, O, C, N and H atoms, respectively.

HM-MS/CN sample after absorbing BPA and after reaction with H_2O_2 are shown in Fig. 6a,b. The spectrum of MoS_2 displays a absorption band at 3455.3 cm^{-1} (Fig. 6a), which is ascribed to the stretching vibrations of OH [ν(OH)] adsorbed on the surface of MoS_2.[26] For HM-MS/CN, the ν(OH) shifted to a lower wavenumber (3430.7 cm^{-1}) due to the coordination of the g-C_3N_4 with the metal Mo species [13,28], forming the cross-linking M-O-C bond bridges. However, the centered band of ν(OH) shifts to a higher wavenumber (3438.0 cm^{-1}) after absorbing BPA on HM-MS/CN, indicating that the electron-rich BPA do not contact with the metal sites, but are mainly adsorbed on the electron-deficient areas of HM-MS/CN throughout the process, which can be clearly demonstrated by the changes of the several organic bands on HM-MS/CN. As shown in Fig. 6b, the peaks at 1399.6 and 1611.7 cm^{-1} are assigned to the skeletal stretching of the C-N heterocycles on HM-MS/CN, which cannot be observed on the pure MoS_2 sample. After absorbing BPA, the intensity of the two peaks is significantly weakened, indicating that BPA is indeed adsorbed on the electron-deficient sites of HM-MS/CN, covering up the characteristic peaks of g-C_3N_4. Actually, the peak at 1618.0 cm^{-1} is largely attributed by the aromatic C=C of BPA. As the reaction progresses with H_2O_2, the organic compounds adsorbed on the electron-deficient sites are gradually degraded, so the wavenumber of ν(OH) gradually returns to a lower value (3433.6 cm^{-1} at 120 min) and the two peaks corresponding to the skeletal stretching of the C-N heterocycles re-emerge and return to their original positions (1611.2 and 1399.6 cm^{-1} at 120 min). These phenomena demonstrate the adsorption and decomposition of the stable organic compounds and H_2O_2 at different polarized sites on HM-MS/CN.

On this basis, we performed the BMPO-trapped EPR technique in the catalyst dispersions to detect the generated •OH and HO$_2^•$/O$_2^{•-}$ radicals and observe the electron transfer processes between the active reaction centers of HM-MS/CN and solution composition factor (H_2O, dissolved O_2, H_2O_2 and organic compounds). The BMPO-•OH species were detected in air-saturated aqueous catalyst dispersions and the BMPO-HO$_2^•$/O$_2^{•-}$ species were detected in methanolic media because the O$_2^{•-}$ radicals in water are very unstable. In the absence of H_2O_2, no BMPO-•OH signal is observed in the HM-MS/CN suspensions with/ without organic compounds (Fig. S8), while four distinct characteristic peaks corresponding to BMPO-HO$_2^•$/O$_2^{•-}$ signal are observed in the HM-MS/CN suspension (Fig. S9). This result suggests that the free electrons accumulated around Mo of HM-MS/CN through π→cation interactions

can directly reduce the dissolved O_2 to HO$_2^•$/O$_2^{•-}$. After adding stable organic compounds (taking BPA as an example), the BMPO-HO$_2^•$/O$_2^{•-}$ signal is obviously enhanced, which indicates that the stable organic compounds can directly act as electron donors to provide more electrons for the electron-deficient sites of HM-MS/CN [34,58]. These electrons are quickly transferred to the Mo centers through π→cation interactions via the twofold cross-linking bridges, enhancing the reduction of the dissolved O_2 to HO$_2^•$/O$_2^{•-}$. In the presence of H_2O_2, four evident characteristic peaks with the intensity of 1:2:2:1 corresponding to BMPO-•OH signal (Fig. 6c) and four stronger peaks corresponding to BMPO-HO$_2^•$/O$_2^{•-}$ signal (Fig. 6d) are observed in the HM-MS/CN suspension, which indicates that H_2O_2 can be efficiently reduced to •OH by the electrons around the electron-rich Mo centers and oxidized to HO$_2^•$/O$_2^{•-}$ in the electron-deficient sites of HM-MS/CN, confirming an excellent activation ability for H_2O_2 over HM-MS/CN. After adding the stable organic compound BPA to the HM-MS/CN/H_2O_2 system, the BMPO-•OH signal intensity has not been weakened but has increased even the partial generated •OH radicals being consumed by the organic compounds (Fig. 6c), indicating that the presence of the organic compounds provide more electron donors to the system and further promote the selective reduction of H_2O_2 (hydroxylation process), which can be verified by the BMPO-HO$_2^•$/O$_2^{•-}$ signals. As shown in Fig. 6d, the BMPO-HO$_2^•$/O$_2^{•-}$ signals are evidently weakened in the HM-MS/CN/H_2O_2 system after adding BPA, which reveals that the organic compounds act as electron donors at the electron-deficient sites, avoiding the oxidation of partial H_2O_2 into HO$_2^•$/O$_2^{•-}$ and accelerating the spontaneous electron transfer cycles that from organic compounds to electron-deficient sites, from electron-deficient sites to electron-rich Mo centers through the π→cation interactions via the twofold cross-linking bridges and from electron-rich centers to H_2O_2 with the generation of •OH and hydroxylation process (Fig. 6e). So, the organic compounds as spontaneous electron donors substituting H_2O_2 consumption via the twofold cation-π is successfully realized in the HM-MS/CN/H_2O_2 system. By quenching •OH and HO$_2^•$/O$_2^{•-}$ with tert-butyl alcohol and *p*-benzoquinone, respectively, the catalytic activity of the HM-MS/CN Fenton-like systems for pollutant degradation were only weakly affected (Fig. S10), suggesting that pollutants were mainly cracked by electron donor effect on the surface of the catalyst, which was the dominant path of water purification, and free radical attack played a secondary role, especially for the removal of RhB.

To verify the above interface reaction mechanism, the intermediate products produced in the reaction process were determined in the HM-MS/CN Fenton-like system. As shown in Fig. 7a, for the degradation of RhB, it is obvious that the GC-MS spectrum shows a series of characteristic peaks of organic substances in the range of 5~35 min, which are adsorbed on the surface of the catalyst or dissociated in the reaction solution, and are partially identified in Table S1. The generation of N,N-diethylformamide, hydroquinone, 2,4-dihydroxybenzoic acid, pyruvic acid and other small molecular intermediates indicates that RhB is progressively oxidized and decomposed through the two pathways involving the dominant π-π interactions and the weaker hydroxylation reactions (Fig. 7a). Similarly, the degradation intermediates of BPA in HM-MS/CN Fenton-like system were also analyzed and identified (Fig. 7b and Table S2). The production of non-hydroxylated products (e. g., benzene) confirms that the electron donation effect of BPA causes its direct decomposition through π-π interactions. Hydroxylation products (e.g., 3,4-dihydroxybutanoic acid, methacrylic acid and ethylene glycol), on the other hand, confirm further attacks by free radicals on intermediates. In addition, all pollutants selected in this study have a common structure feature, that is, benzene ring structures with π-electrons, which are easy to form π-π interactions with the CN ring on the catalyst surface and become a bridge for electron transfers.

4. Conclusions

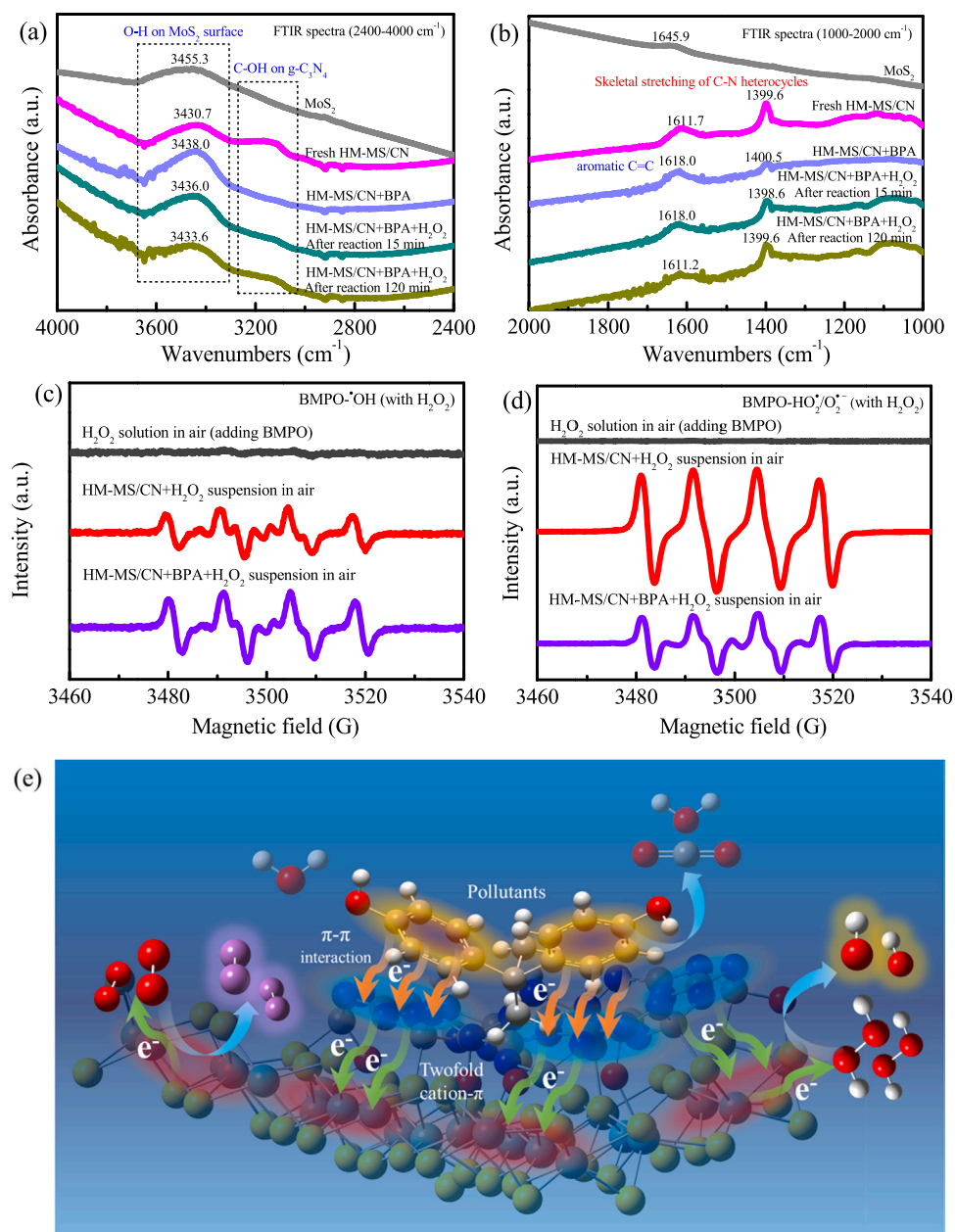In summary, we develop a twofold cation-π-assembled catalyst HM-

Fig. 6. FTIR spectra of pure MoS_2 and HM-MS/CN before and after absorbing BPA or after reaction with H_2O_2 in the range of (a) 2400–4000 cm^{-1} and (b) 1000–2000 cm^{-1}. BMPO spin-trapping EPR spectra for (c) $^{\bullet}OH$ and (d) $HO_2^{\bullet}/O_2^{\bullet -}$ in various suspensions with H_2O_2. (e) Electron donor mechanism of pollutants on catalyst surface.

MS/CN to address the bottleneck of resource and energy consumption in H_2O_2 application industry. EXAFS reveals that the twofold cation-π structures are successfully constructed on HM-MS/CN by forming reinforced electron transfer bonding bridges of Mo-O-C and Mo-S-C. It is found that the electrons of stable organic compounds can be directly captured and converted into activated electrons on the catalyst surface due to the enhanced cation-π interaction under natural air conditions. The obtained electrons from organic compounds are then easily obtained by H_2O_2, which restricts the disproportionation reaction and makes the hydroxylation of H_2O_2 become the dominant reaction. A series of experiments and theoretical calculations were used to illustrate the interface reaction process. This discovery is used in water treatment, enabling refractory pollutants as spontaneous electron donors substituting H_2O_2 consumption via the twofold cation-π interaction. The reaction rate constant for organic pollutant removal in HM-MS/CN suspension is ~39, 102 and 9 times higher than that in the

suspensions of Fe_3O_4, g-C_3N_4 and MoS_2, respectively. A good repeatability and stability (consecutive multiple runs without loss of activity) is also presented. The actual consumption of H_2O_2 in the HM-MS/CN system is only 6–8% of that in the conventional Fenton/Fenton-like systems. The sharp drop in H_2O_2 consumption is of great significance for the application of H_2O_2 in fine chemical industry and environmental remediation.

CRediT authorship contribution statement

Lai Lyu: Conceptualization, Methodology, Investigation, Data curation, Formal analysis, Visualization, Writing – original draft, Funding acquisition. **Chao Lu:** Validation, Data curation. **Yingtao Sun:** Data curation, Visualization. **Wenrui Cao:** Methodology, Formal analysis. **Tingting Gao:** Investigation. **Chun Hu:** Conceptualization, Supervision, Writing – review & editing, Funding acquisition, Project
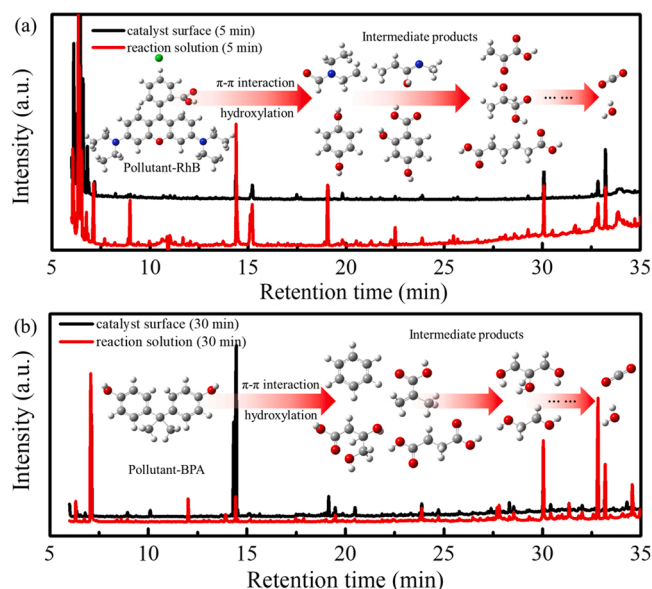
Fig. 7. (a) Analysis of intermediate products of RhB degradation in the HM-MS/CN suspensions with H_2O_2 by GC-MS. (b) Analysis of intermediate products of BPA degradation in the HM-MS/CN suspensions with H_2O_2 by GC-MS. The detailed analysis method of GC-MS is shown in the experimental section.

administration.

Declaration of Competing Interest

The authors declare that they have no known competing financial interests or personal relationships that could have appeared to influence the work reported in this paper.

Data Availability

Data will be made available on request.

Appendix A. Supporting information

Supplementary data associated with this article can be found in the online version at doi:10.1016/j.apcatb.2022.121871.

References

[1] C. Xia, Y. Xia, P. Zhu, L. Fan, H.T. Wang, Direct electrosynthesis of pure aqueous H_2O_2 solutions up to 20% by weight using a solid electrolyte, Science 366 (2019) 226–227.

[2] N.M. Wilson, D.W. Flaherty, Mechanism for the direct synthesis of H_2O_2 on Pd clusters: heterolytic reaction pathways at the liquid-solid interface, J. Am. Chem. Soc. 138 (2016) 574–586.

[3] S. Siahrostami, A. Verdaguer-Casadevall, M. Karamad, D. Deiana, P. Malacrida, B. Wickman, M. Escudero-Escribano, E.A. Paoli, R. Frydendal, T.W. Hansen,

I. Chorkendorff, I.E.L. Stephens, J. Rossmeisl, Enabling direct H_2O_2 production through rational electrocatalyst design, Nat. Mater. 12 (2013) 1137–1143.

[4] J. Xu, Z.Y. Chen, H.W. Zhang, G.B. Lin, H.X. Lin, X.X. Wang, J.L. Long, $Cd_3(C_3N_3S_3)_2$ coordination polymer/graphene nanoarchitectures for enhanced photocatalytic H_2O_2 production under visible light, Sci. Bull. 62 (2017) 610–618.

[5] Y. Li, Y.X. Zhang, G.S. Xia, J.H. Zhan, G. Yu, Y.J. Wang, Evaluation of the technoeconomic feasibility of electrochemical hydrogen peroxide production for decentralized water treatment, Front. Environ. Sci. Eng. 15 (2021) 1.

[6] J.S. Jirkovsky, I. Panas, E. Ahlberg, M. Halasa, S. Romani, D.J. Schiffrin, Single atom hot-spots at Au-Pd nanoalloys for electrocatalytic H_2O_2 production, J. Am. Chem. Soc. 133 (2011) 19432–19441.

[7] Y. Morimoto, S. Bunno, N. Fujieda, H. Sugimoto, S. Itoh, Direct hydroxylation of benzene to phenol using hydrogen peroxide catalyzed by nickel complexes supported by pyridylalkylamine ligands, J. Am. Chem. Soc. 137 (2015) 5867–5870.

[8] K.L. Deng, T.T. Gao, Q. Fang, F.Y. Wu, C. Lu, F. Zhang, W.R. Cao, M.E. Han, C. Hu, L. Lyu, Vanadium tetrasulfide cross-linking graphene-like carbon driving a sustainable electron supply chain from pollutants through the activation of dissolved oxygen and hydrogen peroxide, Environ. Sci. Nano 8 (2021) 86–96.

[9] Y.M. Wang, Q. Fang, Z.J. Xie, C. Hu, L. Lyu, Enhanced Fenton-like process via interfacial electron donating of pollutants over in situ Cobalt-doped graphitic carbon nitride, J. Colloid Interf. Sci. 608 (2022) 673–682.

[10] L. Lyu, C. Hu, Heterogeneous Fenton catalytic water treatment technology and mechanism, Prog. Chem. 29 (2017) 981–999.

[11] C. Lu, K.L. Deng, C. Hu, L. Lyu, Dual-reaction-center catalytic process continues Fenton's story, Front. Environ. Sci. Eng. 14 (2020) 82.

[12] L. Lyu, G.F. Yu, L.L. Zhang, C. Hu, Y. Sun, 4-phenoxyphenol-functionalized reduced graphene oxide nanosheets: a metal-free Fenton-like catalyst for pollutant destruction, Environ. Sci. Technol. 52 (2018) 747–756.

[13] L. Lyu, L.L. Zhang, Q.Y. Wang, Y.L. Nie, C. Hu, Enhanced Fenton catalytic efficiency of γ-Cu-Al_2O_3 by σ-Cu^{2+}-ligand complexes from aromatic pollutant degradation, Environ. Sci. Technol. 49 (2015) 8639–8647.

[14] S.H. Zhan, H.X. Zhang, X.Y. Mi, Y.B. Zhao, C. Hu, L. Lyu, Efficient Fenton-like process for pollutant removal in electron-rich/poor reaction sites induced by surface oxygen vacancy over cobalt-zinc oxides, Environ. Sci. Technol. 54 (2020) 8333–8343.

[15] X.J. Zhang, J.R. Liang, Y. Sun, F.G. Zhang, C.W. Li, C. Hu, L. Lyu, Mesoporous reduction state cobalt species-doped silica nanospheres: an efficient Fenton-like catalyst for dual-pathway degradation of organic pollutants, J. Colloid Interf. Sci. 576 (2020) 59–67.

[16] S.Y. Guvenc, G. Varank, Degradation of refractory organics in concentrated leachate by the Fenton process: central composite design for process optimization, Front. Environ. Sci. Eng. 15 (2021) 2.

[17] S. Xue, S.B. Sun, W.H. Qing, T.B. Huang, W. Liu, C.Q. Liu, H. Yao, W. Zhang, Experimental and computational assessment of 1,4-Dioxane degradation in a photo-Fenton reactive ceramic membrane filtration process, Front. Environ. Sci. Eng. 15 (2021) 95.

[18] Y.S. Zhang, G.K. Li, Y.F. Hu, Fabrication of bimetallic nanoparticles modified hollow nanoporous carbons derived from covalent organic framework for efficient degradation of 2,4-dichlorophenol, Chin. Chem. Lett. 32 (2021) 2529–2533.

[19] D.X. Yang, D. Qu, L. An, X.P. Zong, Z.C. Sun, A metal-free carbon dots for wastewater treatment by visible light active photo-Fenton-like reaction in the broad pH range, Chin. Chem. Lett. 32 (2021) 2292–2296.

[20] S. Navalon, M. de Miguel, R. Martin, M. Alvaro, H. Garcia, Enhancement of the catalytic activity of supported gold nanoparticles for the Fenton reaction by light, J. Am. Chem. Soc. 133 (2011) 2218–2226.

[21] C. Ma, S. Feng, J.M. Zhou, R.F. Chen, Y. Wei, H. Liu, S. Wang, Enhancement of H_2O_2 decomposition efficiency by the co-catalytic effect of iron phosphide on the Fenton reaction for the degradation of methylene blue, Appl. Catal. B Environ. 259 (2019), 118015.

[22] S.Y. Zheng, M.H. Huang, S.M. Sun, H.T. Zhao, L.J. Meng, T.W. Mu, J.L. Song, N. Jiang, Synergistic effect of MIL-88A/g-C_3N_4 and MoS_2 to construct a self-cleaning multifunctional electrospun membrane, Chem. Eng. J. 421 (2021), 129621.

[23] X. Bai, X. Wang, T. Jia, L. Guo, D. Hao, Z. Zhang, L. Wu, X. Zhang, H. Yang, Y. Gong, J. Li, H. Li, Efficient degradation of PPCPs by $Mo_{1-x}S_{2-y}$ with S vacancy at phase-junction: promoted by innergenerate-H_2O_2, Appl. Catal. B Environ. 310 (2022), 121302.

[24] L.X. Sun, X.J. Tan, W.H. Ding, Y.X. Huang, Emerging investigator series: hetero-phase junction 1T/2H-MoS_2 nanosheets decorated by FeOOH nanoparticles for enhanced visible light photo-Fenton degradation of antibiotics, Environ. Sci. Nano 9 (2022) 2342–2350.

[25] L. Lyu, W.R. Cao, G.F. Yu, D.B. Yan, K.L. Deng, C. Lu, C. Hu, Enhanced polarization of electron-poor/rich micro-centers over nZVCu-Cu(II)-rGO for pollutant removal with H_2O_2, J. Hazard. Mater. 383 (2020), 121182.

[26] L. Lyu, M.E. Han, W.R. Cao, Y.W. Gao, Q.Y. Zeng, G.F. Yu, X. Huang, C. Hu, Efficient Fenton-like process for organic pollutant degradation on Cu-doped mesoporous polyimide nanocomposites, Environ. Sci. Nano 6 (2019) 798–808.

[27] L. Lyu, D.B. Yan, G.F. Yu, W.R. Cao, C. Hu, Efficient destruction of pollutants in water by a dual-reaction center Fenton-like process over carbon nitride compounds-complexed Cu(II)-CuAlO₂, Environ. Sci. Technol. 52 (2018) 4294–4304.

[28] L. Lyu, L.L. Zhang, G.Z. He, H. He, C. Hu, Selective H_2O_2 conversion to hydroxyl radicals in the electron-rich area of hydroxylated C-g-C_3N_4/ CuCo-Al_2O_3, J. Mater. Chem. A 5 (2017) 7153–7164.

[29] H.X. Zhang, C.W. Li, L. Lyu, C. Hu, Surface oxygen vacancy inducing peroxymonosulfate activation through electron donation of pollutants over cobalt-zinc ferrite for water purification, Appl. Catal. B Environ. 270 (2020), 118874.

[30] K.L. Deng, Y.T. Gu, T.T. Gao, Z.Y. Liao, Y.X. Feng, S. Zhou, Q. Fang, C. Hu, L. Lyu, Carbonized MOF-coated zero-valent Cu driving an efficient dual-reaction-center Fenton-like water treatment process through utilizing pollutants and natural dissolved oxygen, ACS EST, Water 2 (2022) 174–183.

[31] Z.L. Song, M.X. Wang, Z. Wang, Y.F. Wang, R.Y. Li, Y.T. Zhang, C. Liu, Y. Liu, B. B. Xu, F. Qi, Insights into heteroatom-doped graphene for catalytic ozonation: active centers, reactive oxygen species evolution, and catalytic mechanism, Environ. Sci. Technol. 53 (2019) 5337–5348.

[32] W.R. Cao, C. Hu, L. Lyu, Efficient decomposition of organic pollutants over nZVI/FeO$_x$/FeN$_y$-anchored NC layers via a novel dual-reaction-centers-based wet air oxidation process under natural conditions, ACS EST Eng. 1 (2021) 1333–1341.

[33] X.Z. Chen, W.J. Ong, Z.Z. Kong, X.J. Zhao, N. Li, Probing the active sites of site-specific nitrogen doping in metal-free graphdiyne for electrochemical oxygen reduction reactions, Sci. Bull. 65 (2020) 45–54.

[34] Y. Wang, L. Lyu, D. Wang, H.-Q. Yu, T. Li, Y. Gao, F. Li, J.C. Crittenden, L. Zhang, C. Hu, Cation-π induced surface cleavage of organic pollutants with ·OH formation from H$_2$O for water treatment, iScience 24 (2021), 102874.

[35] C. Grauffel, B.Q. Yang, T. He, M.F. Roberts, A. Gershenson, N. Reuter, Cation−π interactions as lipid-specific anchors for phosphatidylinositol-specific phospholipase C, J. Am. Chem. Soc. 135 (2013) 5740–5750.

[36] H. Yorita, K. Otomo, H. Hiramatsu, A. Toyama, T. Miura, H. Takeuchi, Evidence for the Cation-π interaction between Cu^{2+} and tryptophan, J. Am. Chem. Soc. 130 (2008) 15266–15267.

[37] H.X. Zhang, L. Lyu, Q. Fang, C. Hu, S.H. Zhan, T. Li, Cation−π structure inducing efficient peroxymonosulfate activation for pollutant degradation over atomically dispersed cobalt bonding graphene-like nanospheres, Appl. Catal. B Environ. 286 (2021), 119912.

[38] A. Lagutschenkov, R.K. Sinha, P. Maitre, O. Dopfer, Structure and infrared spectrum of the Ag$^+$-phenol ionic complex, J. Phys. Chem. A 114 (2010) 11053–11059.

[39] X. Tong, S. Wang, J. Zuo, Y. Ge, Q. Gao, S. Liu, J. Ding, F. Liu, J. Luo, J. Xiong, Two 2D uranyl coordination complexes showing effective photocatalytic degradation of Rhodamine B and mechanism study, Chin. Chem. Lett. 32 (2021) 604–608.

[40] P.P. Qiu, T. Zhao, X.H. Zhu, B. Thokchom, J.P. Yang, W. Jiang, L.J. Wang, Y.C. Fan, X.P. Li, W. Luo, A confined micro-reactor with a movable Fe$_3$O$_4$ core and a mesoporous TiO$_2$ shell for a photocatalytic Fenton-like degradation of bisphenol A, Chin. Chem. Lett. 32 (2021) 1456–1461.

[41] Y.T. Gu, T.T. Gao, F.G. Zhang, C. Lu, W.R. Cao, Z.W. Fu, C. Hu, L. Lyu, Surface sulfur vacancies enhanced electron transfer over Co-ZnS quantum dots for efficient degradation of plasticizer micropollutants by peroxymonosulfate activation, Chin. Chem. Lett. 33 (2022) 3829–3834.

[42] M.C. Yu, H.J. Liang, R.N. Zhan, L. Xu, J.F. Niu, Sm-doped g-C$_3$N$_4$/Ti$_3$C$_2$ MXene heterojunction for visible-light photocatalytic degradation of ciprofloxacin, Chin. Chem. Lett. 32 (2021) 2155–2158.

[43] Y. Li, Y.M. Miao, M.Q. Yang, Y.X. Wu, G.Q. Yan, DNA detection based on Mn-doped ZnS quantum dots/methylene blue nanohybrids, Chin. Chem. Lett. 27 (2016) 773–778.

[44] H. Bader, V. Sturzenegger, J. Hoigne, Photometric method for the determination of low concentrations of hydrogen peroxide by the peroxidase catalyzed oxidation of N,N-diethyl-p-phenylenediamine (DPD), Water Res 22 (1988) 1109–1115.

[45] J.M. Wu, W.E. Chang, Y.T. Chang, C.K. Chang, Piezo-catalytic effect on the enhancement of the ultra-high degradation activity in the dark by single- and few-layers MoS$_2$ nanoflowers, Adv. Mater. 28 (2016) 3718–3725.

[46] M.H. Wu, L. Li, Y.C. Xue, G. Xu, L. Tang, N. Liu, W.Y. Huang, Fabrication of ternary GO/g-C$_3$N$_4$/MoS$_2$ flower-like heterojunctions with enhanced photocatalytic activity for water remediation, Appl. Catal. B Environ. 228 (2018) 103–112.

[47] J.K. Song, C.Y. Li, X.J. Wang, S.S. Zhi, X. Wang, J.H. Sun, Visible-light-driven heterostructured g-C$_3$N$_4$/Bi-TiO$_2$ floating photocatalyst with enhanced charge carrier separation for photocatalytic inactivation of Microcystis aeruginosa, Front. Environ. Sci. Eng. 15 (2021) 129.

[48] Y.H. Lee, X.Q. Zhang, W.J. Zhang, M.T. Chang, C.T. Lin, K.D. Chang, Y.C. Yu, J.T. W. Wang, C.S. Chang, L.J. Li, T.W. Lin, Synthesis of large-area MoS$_2$ atomic layers with chemical vapor deposition, Adv. Mater. 24 (2012) 2320–2325.

[49] P.S. Toth, M. Velicky, M.A. Bissett, T.J.A. Slater, N. Savjani, A.K. Rabiu, A. M. Rakowski, J.R. Brent, S.J. Haigh, P. O'Brien, R.A.W. Dryfe, Asymmetric MoS$_2$/graphene/metal sandwiches: preparation, characterization, and application, Adv. Mater. 28 (2016) 8256–8264.

[50] H. Xu, J.J. Yi, X.J. She, Q. Liu, L. Song, S.M. Chen, Y.C. Yang, Y.H. Song, R. Vajtai, J. Lou, H.M. Li, S.Q. Yuan, J.J. Wu, P.M. Ajayan, 2D heterostructure comprised of metallic 1T-MoS$_2$/Monolayer O-g-C$_3$N$_4$ towards efficient photocatalytic hydrogen evolution, Appl. Catal. B Environ. 220 (2018) 379–385.

[51] L. Shi, W. Ding, S.P. Yang, Z. He, S.Q. Liu, Rationally designed MoS$_2$/protonated g-C$_3$N$_4$ nanosheet composites as photocatalysts with an excellent synergistic effect toward photocatalytic degradation of organic pollutants, J. Hazard. Mater. 347 (2018) 431–441.

[52] X.W. Shi, M. Fujitsuka, S. Kim, T. Majima, Faster electron injection and more active sites for efficient photocatalytic H$_2$ evolution in g-C$_3$N$_4$/MoS$_2$ hybrid, Small 14 (2018), 1703277.

[53] M.H. Vu, M. Sakar, C.C. Nguyen, T.O. Do, Chemically bonded Ni cocatalyst onto the S doped g-C$_3$N$_4$ nanosheets and their synergistic enhancement in H$_2$ production under sunlight irradiation, ACS Sustain. Chem. Eng. 6 (2018) 4194–4203.

[54] L. Wang, X. Huang, M.E. Han, L. Ti, Y.W. Gao, Q.Y. Zeng, C. Hu, Efficient inhibition of photogenerated electron-hole recombination through persulfate activation and dual-pathway degradation of micropollutants over iron molybdate, Appl. Catal. B Environ. 257 (2019), 117904.

[55] B. Lassalle-Kaiser, D. Merki, H. Vrubel, S. Gul, V.K. Yachandra, X.L. Hu, J. Yano, Evidence from in situ X-ray absorption spectroscopy for the involvement of terminal disulfide in the reduction of protons by an amorphous molybdenum sulfide electrocatalyst, J. Am. Chem. Soc. 137 (2015) 314–321.

[56] H. Tamura, K. Mita, A. Tanaka, M. Ito, Mechanism of hydroxylation of metal oxide surfaces, J. Colloid Interf. Sci. 243 (2001) 202–207.

[57] X.Y. Zhang, Y.B. Ding, H.Q. Tang, X.Y. Han, L.H. Zhu, N. Wang, Degradation of bisphenol A by hydrogen peroxide activated with CuFeO$_2$ microparticles as a heterogeneous Fenton-like catalyst: efficiency, stability and mechanism, Chem. Eng. J. 236 (2014) 251–262.

[58] T.T. Gao, C. Lu, C. Hu, L. Lyu, H$_2$O$_2$ inducing dissolved oxygen activation and electron donation of pollutants over Fe-ZnS quantum dots through surface electron-poor/rich microregion construction for water treatment, J. Hazard. Mater. 420 (2021), 126579.